Description of the flow in a linear cascade with an upstream cavity
Part 1: Influence of turbulence (draft)

M. Fiore [a,1,*], N. Gourdain [b], J.-F. Boussuge [a], E. lippinois [c]

[a] *CERFACS, Computational Fluid Dynamics team, Toulouse, France*
[b] *ISAE-Supaero, Dpt. of Aerodynamics, Energetics and Propulsion, Toulouse, France*
[c] *Safran Aircraft Engines, Moissy-Cramayel, France*

ABSTRACT

In gas turbines, transitional flows are likely to occur over many components depending on the geometrical arrangement, inlet turbulence and Reynolds number. In the case of a low-pressure turbine, the transition from a laminar to a turbulent boundary layer is generally either a bypass process due to free stream turbulence or a separation-induced transition due to the adverse pressure gradient on the blade. The overall blade losses and the operating point are strongly dependent on the ability to predict this boundary layer state, the size and length of the separation bubble. Therefore, turbomachinery designers require tools which accurately predict the laminar-turbulent transition. The Reynolds Averaged Navier–Stokes (RANS) formalism is currently commonly used due a to relatively low computational cost. Except particular developments, this approach is not suited to predict transition processes. The Large Eddy-Simulation (LES) approach is able to predict transition processes at a higher computational cost making it suitable for low-pressure turbine applications in conjunction with inlet turbulence injection since the free-stream turbulence is generally non-negligible and affect near-wall flow behavior. The present study introduces a description of the flow in a linear cascade with an upstream hub cavity at a Reynolds number representative of low-pressure turbines by three different approaches (RANS, LES and LES with inlet turbulence injection). This study shows the influence of turbulence modelling and turbulence injection at the inlet of the domain on the boundary layer state at hub and shroud modifying the secondary vortices radial migration in the blade passage and the cancelling of suction side separation bubble at high free-stream turbulence. The Kevin–Helmholtz instability at the rim seal interface is also cancelled at high free-stream turbulence.

Keywords:
Large-Eddy simulation
Turbulence injection
Transition process
Low-pressure turbine

1. Introduction

The turbofan is currently the most common and efficient gas turbine architecture in commercial airlines used in conjunction with multi-spool arrangement. The fan at the inlet of the gas turbine that provides most of the thrust is linked to the low-pressure turbine. Due to the relatively large fan diameter and to prevent shocks at its tip, its rotational speed is generally low and consequently low for the low-pressure turbine. In typical operating conditions, the flow over a low-pressure turbine is characterized by a relatively low Reynolds number, among the lowest in the different components of the gas turbine [1]. Based on the chord and maximum blade suction side velocity, the Reynols number is in the order of magnitude of 10^5 for medium sized low-pressure turbines. This value evolves all along the mission of the gas turbine and can differs of a factor five between take-off and cruise [2]. This relatively low Reynolds number can promote the development of a laminar boundary layer over the blade suction side and increase the possibility of a separation-induced bubble [3] compared to a turbulent boundary layer. The experimental study of Abu–Ghannam and Shaw [4] on a flat plate with various upstream turbulence levels and streamwise pressure gradients have shown that the boundary layer may remain laminar under no free-stream turbulence until high Reynolds number typically 3×10^6. However, as soon as the free-stream turbulence level is around Tu $\simeq$ 2–3% that can be commonly observed in turbine main flow path, the boundary layer may become turbulent for the characteristic Reynolds number in low-pressure turbines. The free-stream turbulence promotes early transition processes of the blade boundary layer and potential cancelling of suction side separation bub-

---

* Corresponding author.
  E-mail addresses: fiore@cerfacs.fr (M. Fiore), nicolas.gourdain@isae-supaero.fr (N. Gourdain), boussuge@cerfacs.fr (J.-F. Boussuge), eric.lippinois@safrangroup.com (E. lippinois).
  [1] orcid=0000-0003-1740-4581

2

Nomenclature

Latin letter

$\dot{m}$	mass flow rate [kg.s^{-1}]
ω	specific rate of turbulent dissipation [s^{-1}]
k	turbulent kinetic energy [kg.m^2.s^{-2}]
(x,y,z)	Cartesian coordinates [m]
C_p	pressure coefficient [-]
C_x	axial chord-length [m]
E	energy [kg.m^2.s^{-2}]
H_{NGV}	blade height [m]
Ma	Mach number [-]
Re	Reynolds number [-]
St	Strouhal number [-]
Tu	turbulence intensity [-]
u	velocity [m.s^{-1}]

Greek letters

δ	boundary layer thickness [m]
ϵ	turbulent dissipation [kg.m^2.s^{-3}]
γ	sealing flow angle, $tan^{-1}(u_z/u_x)$ [deg]
κ	artificial viscosity coefficient [-]
σ	standard deviation [-]
τ	turbulence decay characteristic time [s]
ζ	total pressure loss coefficient [-]

Subscripts and superscripts

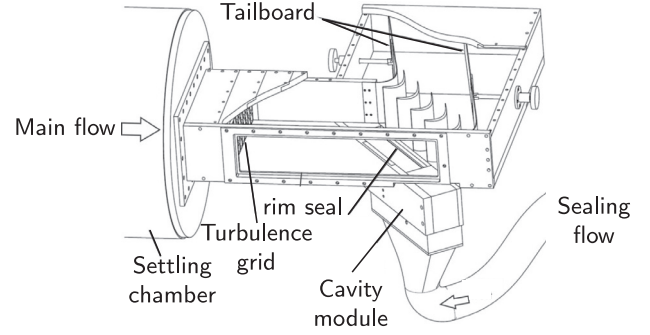|	
∞	upstream conditions
$\bar{.}$	azimuthally averaged quantity
$.'$	fluctuating quantity
$.^+$	non-dimensional wall-units
c	cavity
edge	edge of the boundary layer
m	main annulus
ref	reference state
tot	total quantity
turb	turbulent

Fig. 1. View of the experimental set up. Adapted from Schuler [23].

Table 1
Characteristics of the cascade rig.

cascade details		nominal conditions	
Inlet blade angle	37.9°	Re	5.6 × 10^5
Outlet blade angle	66.3°	Ma	0.22
Axial chord C_x	75 mm	$\dot{m}_m$	1.13 kg.s^{-1}
H_{NGV}/C_x	1.3	$p_{tot,in}$ / p_{out}	1.035
Pitch/C_x	0.884	$\dot{m}_c$ / $\dot{m}_m$	0, 0.5, 1%

ble due to a turbulent nature of the boundary layer [5]. The radial migration of secondary flows developing in the passage are also impacted when hub or shroud boundary layer nature are modified [6]. These different interaction processes between Reynolds number effect, adverse pressure gradient and free-stream turbulence become more and more important to be understood to develop future turbines. Indeed, the current design trend with gearboxed engines that aim at reducing the number of airfoils per row for the same performance (High Lift (HL) and even Ultra High Lift (UHL) blades) [7] will promote higher adverse pressure gradients experienced by the flow as well as potential higher free-stream turbulence due to reduced inter-stage gaps. The Computational Fluid Dynamics (CFD) tool can give insight in the near-wall behavior of gas turbine. The most common and computationally affordable approach is the Reynolds Averaged Navier Stokes (RANS) formalism. Some models have been developed taking into account the transition process in RANS including the one of Jones and Launder [8]. This model introduces the turbulent kinetic energy gradients in the so-called low-Reynolds number versions of the k-ϵ model allowing to handle transition without a dedicated transition model as for the $\gamma - Re_\theta$ model developed by Menter et al. [9]. However, these approaches are scarcely able to capture transition processes in gas turbine context. The Large Eddy Simulation (LES) [10] approach is able, for sufficient grid and near-wall refinement levels to handle the transition process from a laminar to a turbulent regime [1] without additional transition modelling steps. Furthermore, the Reynolds number in low-pressure turbine
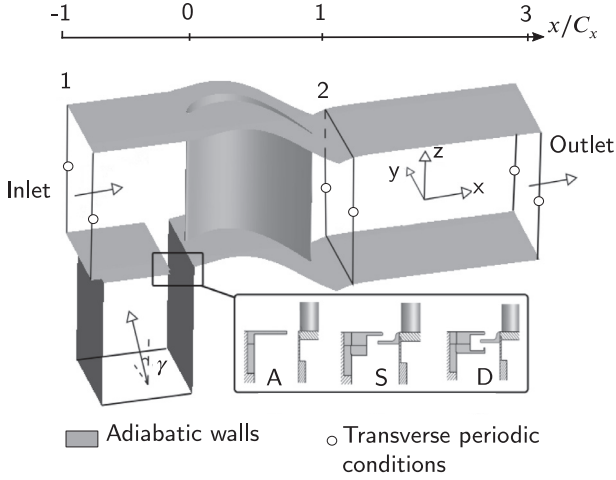
is low enough such that Direct Numerical Simulation (DNS) approach [11–13] or LES [14–16] would be used at a high but more and more affordable computational cost [17,18] in conjunction with turbulence injection to provide representative inlet conditions [19–22].

This paper describes the flow in a linear cascade with an upstream cavity at a Reynolds numbers representative of a low-pressure turbine based on RANS, wall-resolved LES simulation with or without inlet turbulence injection. A special emphasis is given to better understand the influence of turbulence modelling (RANS or LES) and turbulence injection at the inlet for LES on the flow behavior. The first part of this paper introduces the configuration and the numerical setup. The simulations performed are then compared against available experimental data with a focus on the physical roots of the discrepancy between the different simulations performed and the experiments. Once discussed, the analysis of the physical phenomena in the linear cascade are described for the LES with turbulence injection which is the most representative of the experimental test case. Finally, conclusions on the study are drawn.

2. Configuration and numerical methods

2.1. Linear cascade experimental setup

The configuration under study is a low-Mach linear cascade composed of five nozzle guide vane installed at Karlsruhe University, Germany (see Fig. 1). The rig is set in an open circuit which includes an upstream honeycomb settling chamber, a centrifugal blower and a Venturi pipe in order to target the desired inflow conditions. Upstream of the blade leading edge, the rim seal is included in a cavity module linked to the test section allowing to easily set different rim seal designs. The purge flow is supplied to the cavity (c) as a fraction of the mainstream flow (m), respectively $\dot{m}_c/\dot{m}_m = 0$, 0.5 or 1%. Main rig characteristics are gathered in Table 1.

In order to promote periodic conditions on the lateral sections of each blade of the cascade, adjustable tailboards were moved along rig channel's wall. Their position was moved until a low discrepancy for the pressure distribution around the blade for the three inner blade was reached. The tolerated pressure coefficient mismatch at midspan was set to 1 %. This requirement is neces-
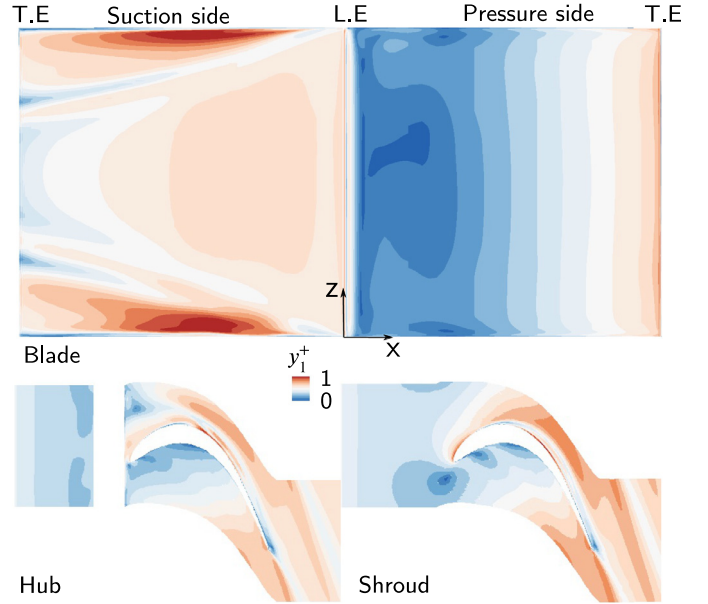
2

Fig. 2. Simulation domain.

Fig. 3. y_1^+ distribution around the wetted surfaces: unwrapped blade (top), hub and shroud (bottom) for the RANS simulation (configuration A05). LE and TE stand respectively for leading and trailing edge.

sary to ensure that the comparison with numerical simulations for which only the central blade is simulated and periodic conditions are applied on the lateral sections is compliant. Three different rim seal geometries are studied experimentally including an axial clearance (A) and two geometries using axial overlapping: simple (S) and double (D) (see Fig. 2). In this paper, the different cases studied with the different geometries and purge flow rates will be denoted by a letter for the rim seal geometry considered (A: axial, S: simple overlapping, D: double overlapping) and a figure for the purge flow rate imposed (0: 0%, 05: 0.5%, 1: 1%). For example, the configuration A05 stands for the axial rim seal geometry with 0.5% of the mainstream flow supplied in the cavity. Total pressure, temperature, azimuthal and radial angles profiles are provided at one axial chord length upstream of the blade leading edge by the experiments. The free-stream turbulence is produced by a turbulence grid positioned at seven axial chord length upstream of the blade leading edge and a turbulent intensity of Tu = 6% at the blade leading edge was measured.

2.2. Numerical parameters

The RANS and LES without inlet turbulence injection (LES1$_{no.inj.}$) simulations have been performed using the Onera code elsA [24] which solves the compressible Navier-Stokes equations over multi-block structured grids. For the RANS simulation, the topology for the nozzle guide vane is built to have a minimal orthogonality higher than $30°$ and a maximal aspect ratio lower than 1,000. In the near-wall regions, these criteria are checked to be higher than $80°$ for orthogonality, lower than 500 for aspect ratio and 1.2 for the expansion ratio. The first off-wall point y_1 is set to $y_1/C_x = 7 \times 10^{-4}$ in order to reach the quality requirements for a wall-resolved simulation $y_1^+ < 1$. Fig. 3 shows y_1^+ distribution around the blade, at the hub and shroud obtained from the RANS simulation. y_1^+ remains below unity for the different wetted surfaces. The mesh is refined at the blade leading and trailing edges, in the wake region and at the interface between the cavity and the main annulus. The mesh is composed of around 7×10^6 cells for the different geometries.

For the LES1$_{no.inj.}$, the expansion was set to 1.03 to ensure around 30 grid points in the viscous layer until $y^+ = 50$. The minimum orthogonality remains higher than $30°$ with values around $80°$ in the near-wall regions. The aspect ratio is also decreased compared to the RANS approach by applying the criteria furnished in the literature to fulfil the recommendation for wall-resolved LES [25–27]. These criteria were set to $50 \leq \Delta x^+ \leq 80$; $y_1^+ \leq 1$;
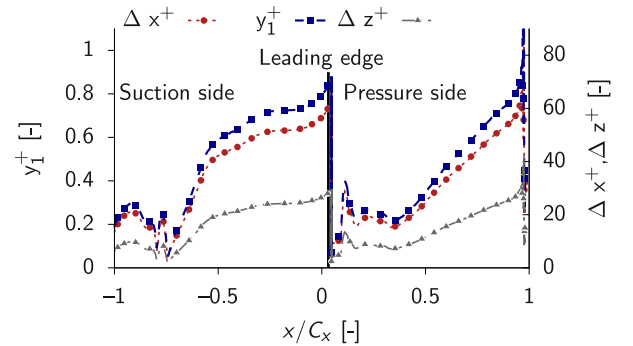
Fig. 4. Midspan averaged grid dimension at wall for the LES1$_{no.inj.}$, configuration A05.

$15 \leq \Delta z^+ \leq 25$ leading to a mesh of around 60×10^6 cells (see Fig. 4). The in-house unstructured AVBP solver [28] is used to perform an additional LES simulation without turbulence injection (LES2$_{no.inj.}$) to assess the validity of the two LES and the simulation with inlet turbulence injection (LES2$_{turb.inj.}$). A layer of 20 prisms in near-wall regions is applied with an expansion ratio of 1.03 and a maximum $y_1^+ \simeq 2$–3 on the blade suction side. Tetrahedra elements fill the remaining domain. A grid refinement from the inlet to the blade leading edge is applied to transport turbulent structures generated at the inlet leading to a mesh of around 80×10^6 cells.

For the RANS simulation, an upwind Roe scheme with third-order limiter [29] is used for the convective terms. The Wilcox k-ω two-equations model with Zheng's limiter [30] is used according to the practice provided by Gourdain et al. [31,32] in a turbomachinery context. For the LES1$_{no.inj.}$, a second order centred scheme with a low Jameson artificial viscosity [33] ($\kappa_{jam.}^4 = 0.002$) is used. The temporal integration is achieved with a Dual Time Step (DTS) approach based on an implicit backward Euler scheme with sub-iterations Newton's algorithm [34] (second order accurate). The time step Δt is adapted to the mesh resolution close to the wall $\Delta t^+ = \Delta t u_\infty/C_x = 10^{-5}$ (i.e. 1 500 time steps per axial chord length). The Sub-Grid Scale model (SGS) is the Wall-Adapting Local

Table 2

Numerical setup for the different numerical approaches.

| Numerical approach	Convective scheme	Temporal scheme	Turbulence model/SGS
RANS elsA	Upwind (3rd order)	DTS	k-ω Wilcox
LES elsA (LES1$_{no.inj.}$)	Centred Jameson ($\kappa^4_{jam.}$=0.002)	DTS ($\Delta t^+ = 10^{-5}$)	WALE
LES AVBP (LES2$_{no.inj.}$/ LES2$_{turb.inj.}$)	TTGC (3rd order)	Explicit (CFL=0.7) $\Delta t^+ \simeq 10^{-6}$	WALE

Eddy-viscosity model (WALE) [35]. For the LES solver AVBP used to run the additional LES simulation without (LES2$_{no.inj.}$) and with turbulence injection (LES2$_{turb.inj.}$), the convective operator is discretized by the two-step Taylor–Galerkin scheme [36] (3rd order accurate). The simulation time step based on the explicit time advancement is $\Delta t^+ \simeq 10^{-6}$. A summary of the numerical parameters is given in Table 2 and a mesh dependency for the different numerical simulations performed is proposed in Appendix A.

2.3. Inlet turbulence injection in LES

Inlet turbulence injection is made in conjunction to Navier–Stokes Characteristic Boundary Conditions (NSCBC) [37] (see Fig. 5a). Velocity fluctuations are generated using a synthetic eddy-viscosity method proposed in Smirnov et al. [38]. The integral length scale is set to 7 mm based on experimental measurements for similar grid and distance to the cascade [39] and numerical study from Segui [40]. This parameter drives the turbulence decay rate since inversely proportional to the integral length scale and the transition processes since the bypass process is highly sensitive to the integral length scale [41]. The cut-off length scale is set to 0.2 mm and corresponds to the characteristic length scale of the mesh at the inlet to the blade. The turbulence spectrum is based on the one proposed by Passot and Pouquet [42]. Once generated, turbulence experiences a spatial decay in the axial direction. The decay of turbulence is compared to the analytical law resulting from the decay of a homogeneous isotropic turbulent field [43] in order to reach similar values of turbulence intensity at the blade leading edge compared to the experiments. The analysis is based on the initial turbulent kinetic energy $E_{k_{turb}}(t_0)$ and initial turbulent dissipation at the inlet of the domain $\epsilon_{k_{turb}}(t_0)$. The time evolution of $E_{k_{turb}}$ is:

$$E_{k_{turb}}(t) = E_{k_{turb}}(t_0)\left(1 + \left(C_{\epsilon_{k_{turb}}} - 1\right)\frac{t}{\tau_0}\right)^{\left(-\frac{1}{C_{\epsilon_{k_{turb}}}-1}\right)} \quad (1)$$

with $\tau_0 = (E_{k_{turb}}(t_0)/\epsilon_{k_{turb}}(t_0))$ and the analytical model constant $C_{\epsilon_{k,turb}} = 1.92$. From the integral length scale, the initial turbulent dissipation is estimated at $\epsilon_{k_{turb}}(t_0) = 2.1 \times 10^6$. The time evolution can then be transformed to a spatial evolution along a streamline using the Taylor hypothesis [43], i.e $x = u_0 t$ with u_0 the velocity at the inlet. Fig. 5b shows the turbulent kinetic energy decay from the inlet of the domain in $x/C_x = -1$ to the blade leading edge (LE) $x/C_x = 0$ obtained by integrating the turbulent kinetic energy on axial planes. The turbulence decay is stronger in the simulation compared to the theoretical one. This can be due to two effects: turbulence is not initially a homogeneous and isotropic turbulence (HIT) in the synthetic eddy viscosity method and some extent is required to reach this state. Also, part of the structures are possibly dissipated by numerics (spatial scheme and sub-grid scale model). The ratio $E_{k_{turb}}(x)/E_{k_{turb}}(0)$ at the blade leading edge is around 0.2 meaning that the velocity fluctuation is around $u'_{LE}/u'_{inlet} = 0.4$. The turbulent fluctuations injected at the inlet of the domain have been set to Tu $\simeq 15\%$ to reach the turbulence level at the blade leading edge measured experimentally Tu $= 6\%$. The value of the turbulence intensity at the blade leading edge has been checked by setting a probe giving a turbulence intensity of 6.5%.


(a)

(b)
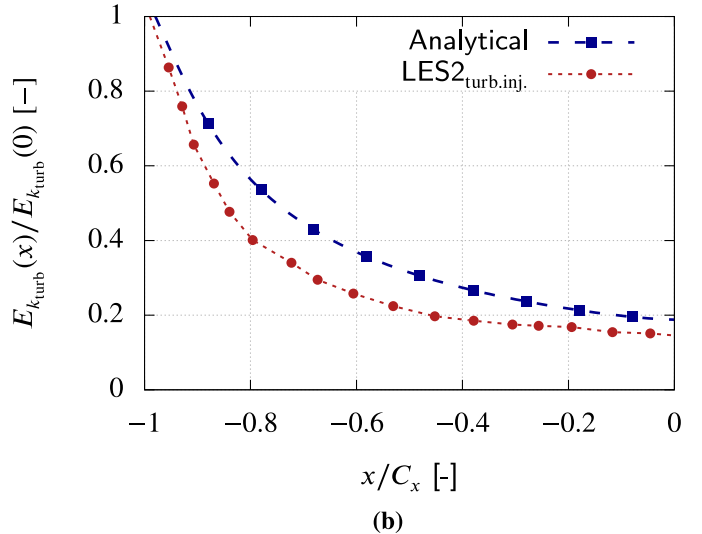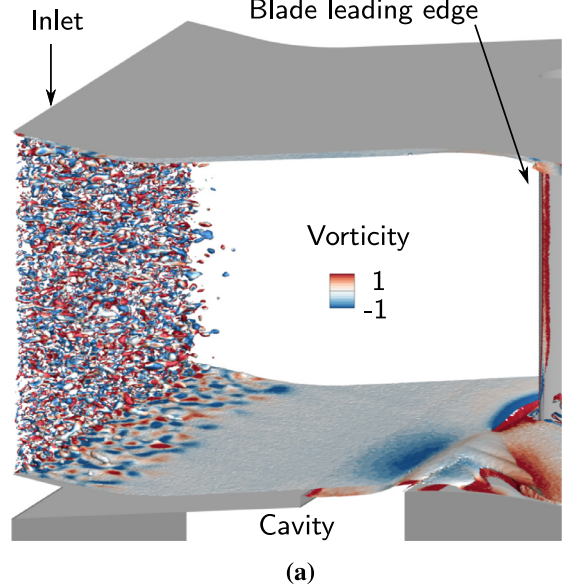
Fig. 5. Iso q-criterion $q = 10^7$ colored by the vorticity showing the turbulence injection at the inlet of the domain in the first time steps (a) and the turbulent kinetic energy decay from the inlet of the domain to the blade leading edge based on a theoretical HIT decay and obtained in the simulation LES2$_{turb.inj.}$ (b), configuration A05.

3. Numerical/experimental comparison

Experimental results available are focused on the main annulus and the comparison with numerical approaches is made on the axial clearance at an intermediate purge flow rate (A05 configuration). The pressure coefficient C_p around the central blade at 4 and 50% blade height (H$_{NGV}$) and pressure loss coefficient downstream of the blade ζ are used for the comparison. These two quantities
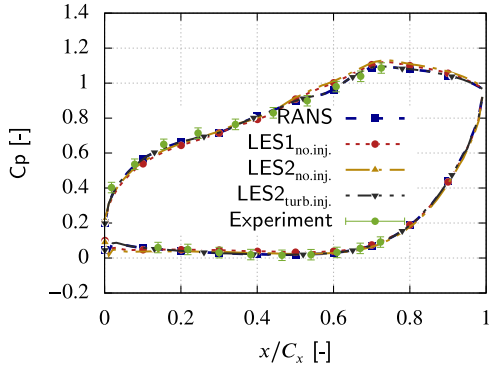
Fig. 6. Pressure coefficient around the blade at 4% blade height for the different numerical approaches and experiments (configuration A05).
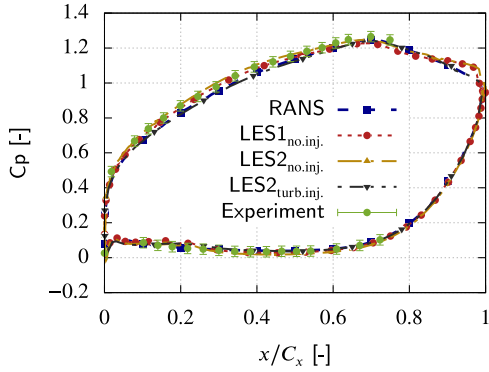
Fig. 7. Pressure coefficient around the blade at 50% blade height for the different numerical approaches and experiments (configuration A05).

are defined as follows

$$C_p(x,z) = \frac{\overline{p}_{tot,1}(z) - p_{blade}(x,z)}{\overline{p}_{tot,2}(z) - \overline{p}_2(z)}, \quad (2)$$

$$\zeta(z) = \frac{\overline{p}_{tot,1}(z) - \overline{p}_{tot,2}(z)}{\overline{p}_{tot,2}(z) - \overline{p}_2(z)}. \quad (3)$$

The overline ⁻ indicates that pressure is pitch-wise area averaged. Subscripts 1 and 2 refer respectively to a position one axial chord upstream of the blade leading edge and 25% downstream of the blade trailing edge. The experimental uncertainty was estimated to be $C_p \pm 0.03$ for the pressure coefficient around the blade and $\zeta \pm 0.015$ for the pressure loss downstream of the blade.

3.1. Cross-validation of LES approaches

The two LES simulations without inlet turbulence injection (LES1$_{no.inj.}$ and LES2$_{no.inj.}$) are first compared based on the pressure coefficient around the blade and pressure loss downstream of the blade to assess the validity of the two LES approaches based on a cross-comparison. The two simulations show a very good matching for the pressure coefficient around the blade close to the hub ($z/H_{NGV} = 4\%$) and at midspan (see red and dark yellow curves in Figs. 6 and 7). For the pressure loss coefficient downstream of the blade, the two simulations show a low discrepancy below 5% (see Fig. 8) with the two main loss peak at $z/H_{NGV} = 20\%$ and $z/H_{NGV} = 80\%$ in good agreement. In addition, the mean flow field has also been analysed for the two simulations and the low discrepancy indicates that despite different meshing strategies and numerical parameters, the two simulations may be used without questioning the approach. In the following, since these two simulations are in good agreement and the inlet turbulence injection is performed with the LES2$_{turb.inj.}$, only the LES2$_{no.inj.}$ will be used
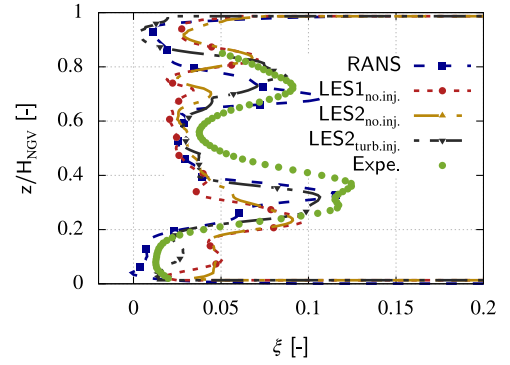
Fig. 8. Pressure loss coefficient downstream of the blade (25% C_x) for the different numerical approaches and experiments (configuration A05).

as the LES simulation with homogeneous inlet conditions for the comparison against experiments and analysis of the flow field.

3.2. Comparison with experimental data

The pressure coefficient close to the hub on the blade suction side is well predicted by the different numerical approaches on the favourable pressure gradient portion of the blade until $x/C_x = 0.7$ corresponding to the throat where experimental results are available. On the diffusion portion downstream of the throat, the different numerical approaches show low discrepancy. On the pressure side a similar agreement with experiments can be observed with a maximum discrepancy around 2%. At midspan, a similar agreement with experimental data can be observed. However, LES2$_{no.inj.}$ shows a lower recompression on the diffusion portion of the blade compared to the RANS and LES2$_{turb.inj.}$.

Regarding the pressure coefficient downstream of the blade, the two main regions of pressure loss at $z/H_{NGV} = 0.35$ and 0.7 are well predicted by RANS and LES2$_{turb.inj.}$ both in terms of amplitude and position with maximum discrepancy of around 8%. LES2$_{no.inj.}$ shows a strong discrepancy compared to the experimental data with lower radial migration and amplitude (locally lower of around 30%) at the two main loss regions. In the following Section 4, the RANS, LES2$_{no.inj.}$ and LES2$_{turb.inj.}$ simulations are analysed to explain the discrepancy between the different approaches.

4. Analysis of the numerical comparison

4.1. Near-wall blade flow

Figs. 9 and 10 show the boundary layer profiles on the forward and rear portions of the blade for the different simulation performed. The positions where the boundary layer profiles have been extracted are given in Fig. 11.

The boundary layer profiles are compared against the Blasius analytical profile solution of the steady two-dimensional Prandtl equation in laminar regime for the LES2$_{no inj.}$.

For the RANS and LES2$_{turb.inj.}$, a power-law boundary layer profile [44] representative of a turbulent boundary layer $(u/u_{edge}) = (y/\delta)^{1/7}$ is used. The wall-normal coordinate and velocity in the boundary layer have been non-dimensionalized by the boundary layer thickness δ and velocity at the edge of the boundary layer u_{edge}. The boundary layer profile for the RANS simulation in the forward part of the blade suction side shows that the boundary layer can be considered as turbulent with a shifted profile due to the favourable pressure gradient. For the LES2$_{turb.inj.}$, the boundary layer profile matches the analytical turbulent boundary layer profile. For the LES2$_{no inj.}$, the boundary layer profile shows a good agreement with the laminar boundary
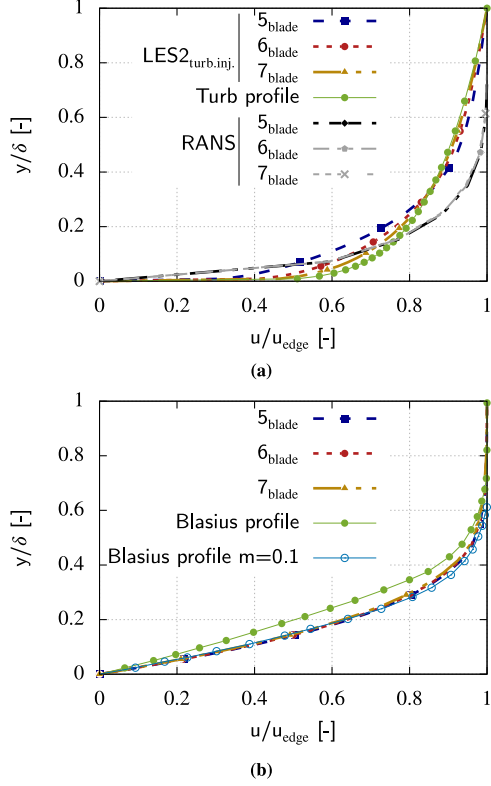
Fig. 9. Boundary layer profiles on the blade suction side in the favourable pressure gradient portion for the RANS/LES2$_{turb.inj.}$ (a) and the LES2$_{no.inj.}$ (b) (configuration A05), see positions 5, 6 and 7 in Fig. 11.
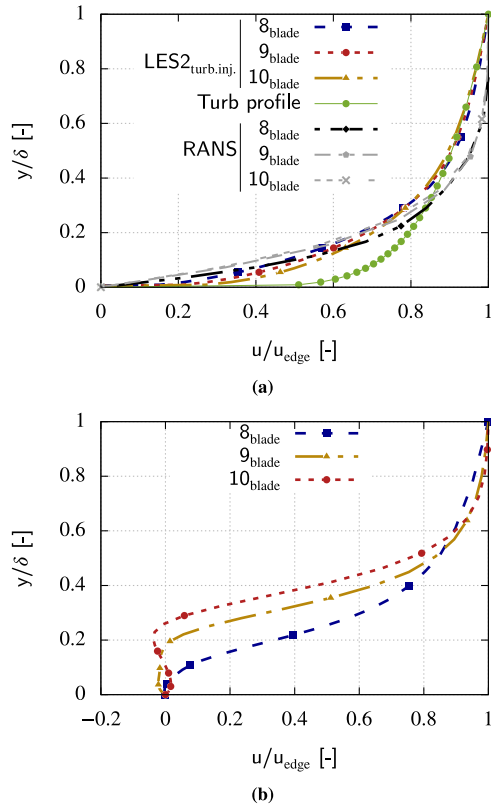
Fig. 10. Boundary layer profiles on the blade suction side in the adverse pressure gradient portion for the RANS/LES2$_{turb.inj.}$ (a) and the LES2$_{no.inj.}$ (b) (configuration A05), see positions 8, 9 and 10 in Fig. 11.
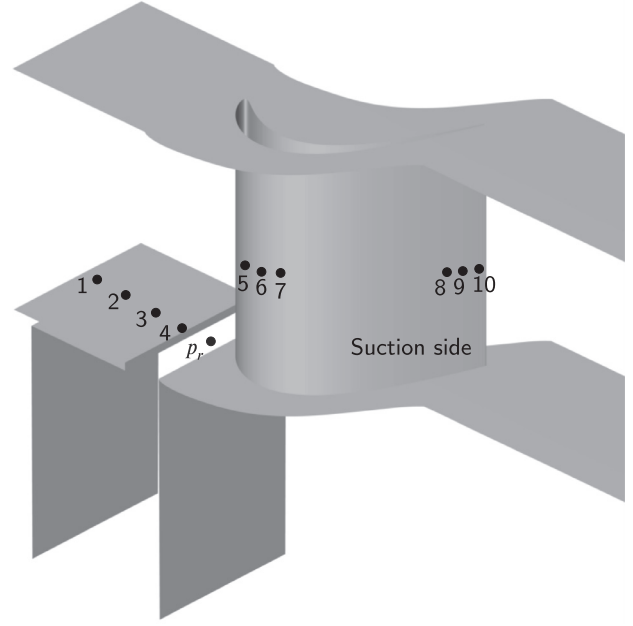
Fig. 11. Boundary layer profiles extraction position for the numerical simulations and probe position (p$_r$).

layer profile with a favourable pressure gradient (m = 0.1).[2] On the rear region of the blade, the boundary layer profile for the RANS and LES2$_{turb.inj.}$ is shifted from the wall due to the adverse pressure gradient but remains attached. For the LES2$_{no.inj.}$, a profile inversion indicates a boundary layer separation. This is characteristic of some low-pressure turbine where at relatively low Reynolds number and/or turbulence level, the boundary layer may remain laminar on the blade suction side and is more prone to separate compared to a turbulent boundary layer [5,45,46]. A similar flow topology around the blade suction side with a separation bubble on the aft portion of the blade was obtained by Hodson and Dominy [47] in the experimental study of a linear cascade with similar blading, lower Reynolds number (290,000), higher Mach number (Ma = 0.7) and low free-stream turbulence (0.5%). This boundary layer separation is characterized by a constant pressure region for the LES2$_{no.inj.}$ compared to the RANS/LES2$_{turb.inj.}$ observed in the comparison of pressure coefficient around the blade at midspan.

4.2. Secondary vortices in the blade passage

Regarding the difference of pressure loss coefficient downstream of the blade for the different simulations performed, some information can be obtained from the secondary vortices developing in the inter blade channel.

The boundary layers developing on the hub and shroud platforms separate when approaching the blade leading edge due to the potential effect. This induces the formation of horse shoe vortices split by the blade leading edge in suction side and pressure side legs. The pressure side leg travels in the inter-blade channel due to the cross pressure gradient while the suction side leg travels on the blade suction side. The two legs merge on the blade suction side and initiate the development and migration of the passage vortex at hub and shroud [48–50] (see Fig. 12). These two vortices are associated to strong entrainment and mixing effects that induce pressure losses and correspond to the two main loss peaks

---

[2] The value of m corresponds to the power value of velocity at the edge of boundary layer u$_{edge}$ = x^m before being injected in the boundary layer equations
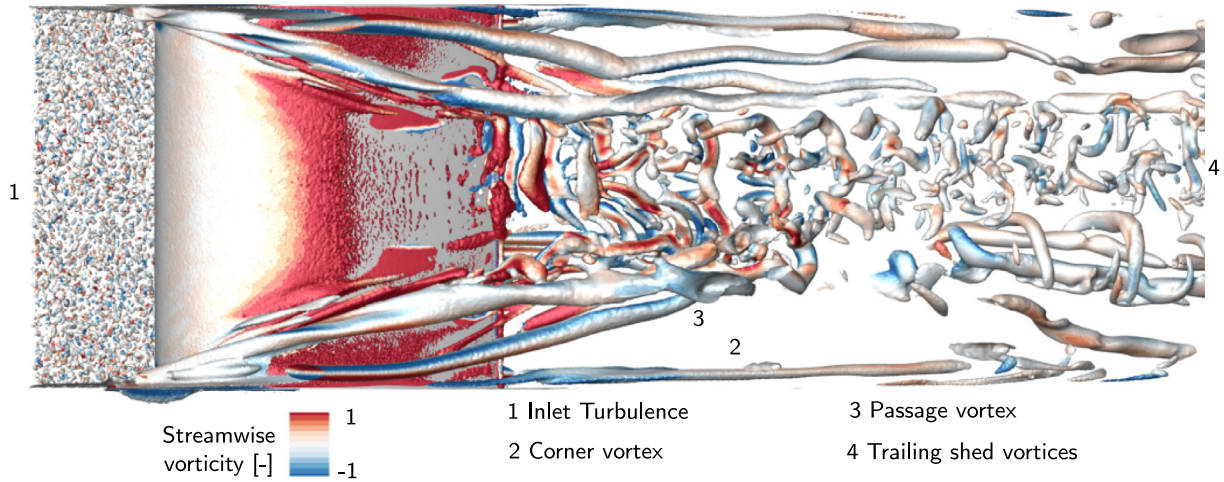
Fig. 12. Lateral sight of blade suction side with iso q-criterion $q = 10^6$ colored by streamwise vorticity for the LES2$_{turb.inj.}$, configuration A05.
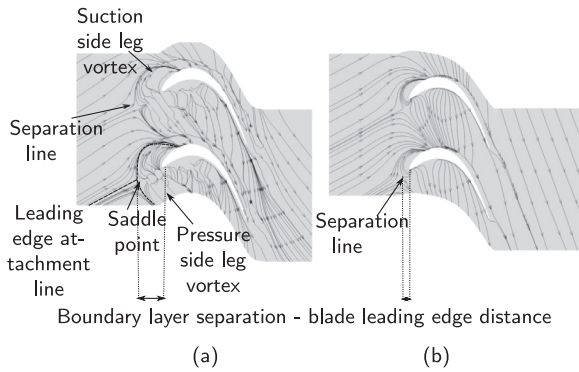

Fig. 13. Time averaged streak lines at the shroud including the boundary layer separation distance from blade leading edge for LES2$_{no inj.}$ (a) and LES2$_{turb.inj.}$ (b), configuration A05.

Fig. 14. Inlet hub boundary layer profiles for RANS/LES2$_{turb.inj.}$ (a) and LES2$_{no.inj.}$ (b) (configuration A05), see positions 1, 2 3 and 4 in Fig. 11.

observed downstream of the nozzle guide vane in the comparison of the different simulations against experiments. When analysing the separation point of the hub/shroud boundary layer, some differences can be exhibited between RANS/LES2$_{turb.inj.}$ and LES2$_{no inj.}$: the boundary layer for LES2$_{no inj.}$ separates upstream compared to the RANS/LES2$_{turb.inj.}$ (see Fig. 13). Fig. 14 shows boundary layer profiles on the hub platform for the different simulations performed. The boundary layer at the hub for the RANS/LES2$_{turb.inj.}$ simulations indicates a profile close to a turbulent one with slight additional momentum close to the wall (see Fig. 14a). For the LES2$_{no inj.}$, the boundary layer profile is close to a laminar boundary layer profile over a flat plate (see Fig. 14b).

The turbulent boundary layer is more resistant to an adverse pressure gradient imposed by the blade potential effect since the fluctuating velocities in the turbulent boundary layer greatly increase the transfer of momentum and energy towards the wall. The turbulent boundary layer is consequently less prone to separate when facing an increasing stagnation pressure due to the blade compared to a laminar boundary layer as stated by Cui et al. [6]. Therefore, the horse shoe vortex process is given an early start for the LES2$_{no.inj.}$ compared to the RANS/LES2$_{turb.inj.}$.

A main consequence is that the radial migration of the passage vortices at hub and shroud is lower (see Fig. 15). Since the two main loss pressure region downstream of the blade can be associated to the passage vortices at hub and shroud, the lower radial migration of the two main loss pressure loss peak downstream of the blade for LES2$_{no inj.}$ can be attributed to the tur-
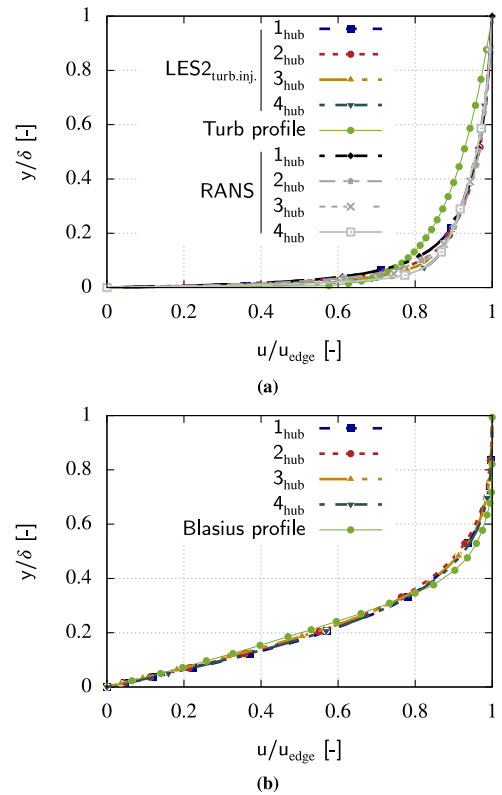
bulent nature of the hub/shroud boundary layer in the experiments while laminar in the LES2$_{no inj.}$. The work of Abu-Ghanam and Shaw [4] on the transitional Reynolds number of the boundary layer over a flat plate depending on the free-stream turbulence can provide informations on the near-wall flow behavior. From a simplified view, the boundary layer transition processes over hub, shroud and blade suction side can be considered as the one occurring over a flat plate.[3] At no free-stream turbulence, the boundary layer may remain laminar until Reynolds number typically equal to

---

[3] The surface roughness, free-stream turbulence characteristics, pressure and curvature effects may have significant effect on the transition process between the flat plate experiment and current configuration but the experiment by Abu-Ghannam
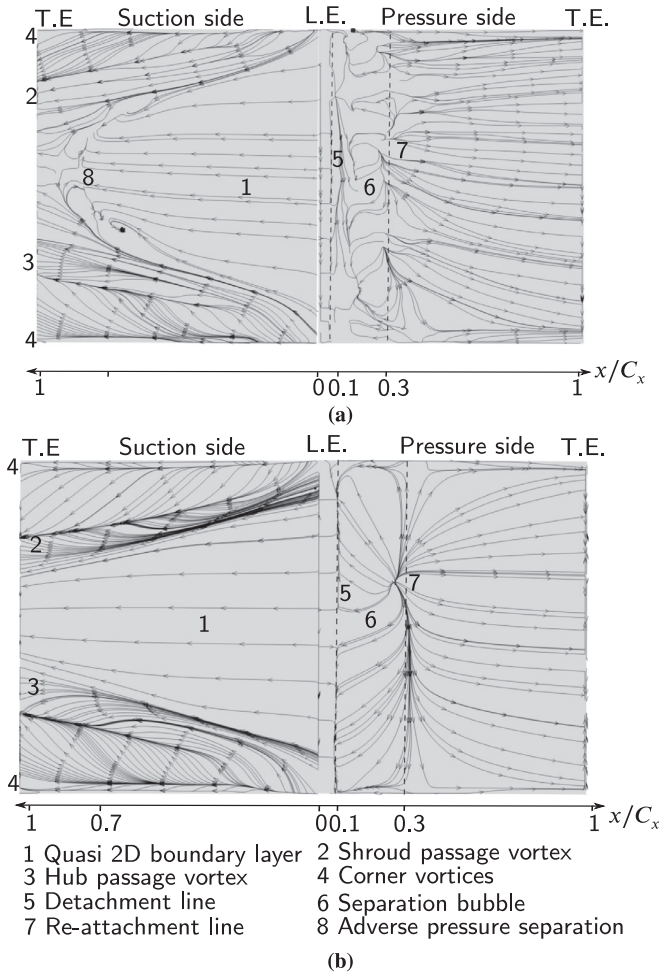
1 Quasi 2D boundary layer 2 Shroud passage vortex
3 Hub passage vortex   4 Corner vortices
5 Detachment line   6 Separation bubble
7 Re-attachment line   8 Adverse pressure separation

(b)

Fig. 15. Streak lines on the suction and pressure side for LES2$_{no\,inj.}$ (a) and LES2$_{turb.inj.}$ (b) (unwrapped blade), configuration A05.

3×10^6. As soon as 2–3% of free-stream turbulence, the transitional Reynolds number is decreased of around one order of magnitude. In current configuration with characteristic Reynolds number Re = 500,000, a free-stream turbulence level of 6% is sufficient to promote a turbulent boundary layer on the hub an shroud. This explains the better behavior of RANS/LES2$_{turb.inj.}$ compared to the LES2$_{no\,inj.}$. Around the blade suction side, the boundary layer becomes quickly turbulent close to the leading edge under a bypass process and no separation bubble on the rear portion is observed compared to the LES2$_{no\,inj.}$. From these observations, it can be concluded that the LES2$_{no\,inj.}$ fails to represent the flow in the linear cascade due to uniform inflow conditions that keep hub, shroud and blade boundary layer laminar. A better agreement is obtained for the RANS approach due to the turbulent nature of the different boundary layers. The best agreement is obtained for the LES2$_{turb.inj.}$ since it matches the inlet boundary conditions of the experiments and there is a fine agreement with the experimental results. Therefore, the LES2$_{turb.inj.}$ is used to describe the flow in the linear cascade with upstream hub cavity in the next Section 5 including RANS/LES2$_{no\,inj.}$ results when turbulence modelling/injection modify the flow behavior.

_____

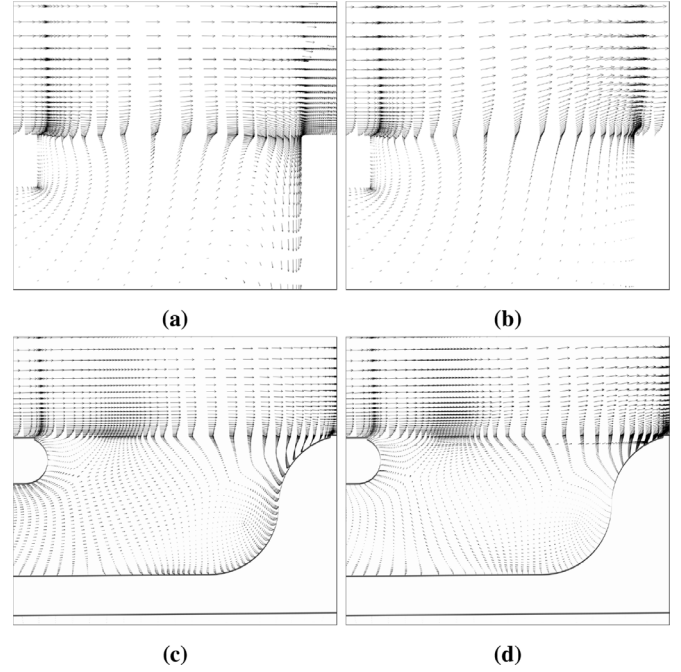and Shaw [4] provides generally a good estimate for the transition Reynolds number

Fig. 16. Velocity vector close to the rim seal: face to leading edge (a)(c) and at the center of the channel (b)(d) for the A05 and S05 configuration based on LES2$_{turb.inj.}$.

## 5. Study of the flow field

5.1. Rim seal flow

The boundary layer developing on the hub platform separates at the rim seal left corner. The velocity gap between the main annulus flow close to the hub and the cavity flow is filled over a short layer typically in the order of magnitude of the incident boundary layer at the rim seal interface (see velocity vector map for the simple gap (A) and simple overlapping (S) rim seal geometries in Fig. 16).

This localized region of velocity adaptation between the cavity and main annulus flow is a shear layer in both axial and azimuthal velocity components since the flow at the inlet was introduced with an azimuthal component that mimic the flow downstream a rotor row. The velocity gap at the interface is shown to be reduced for overlapping geometries compared to simple gap. The axial overlapping arms of these more complex geometries promote a more intense localized recirculation zone that reduce the velocity gap compared to the simple gap geometry. Under no free-stream turbulence as for the homogeneous LES simulation (LES2$_{no\,inj.}$), the shear layer promotes the development of vortical structures that can be associated to the development of a Kelvin–Helmholtz (KH) instability (see Fig. 17).

A three-dimensional Dynamical Mode Decomposition (DMD) [51] has been performed using fully three-dimensional snapshots in time and made possible to isolate a few modes initiated at the rim seal interface and considered as the instability. The spatial reconstruction of this mode can be seen in Fig. 18 characterized by alternating positive and negative density modes around the mean density value at the rim seal interface.

The Kelvin–Helmholtz instability that was developing at the rim seal interface in the LES2$_{no\,inj.}$ is not observed in the case with turbulence injection since no rolling up process is observed. In addition, a probe has been set at the rim seal interface for both simulations. While the Power Spectral Density (PSD) of the LES2$_{no\,inj.}$ shows the peak associated to the Kelvin–Helmholtz instability, no amplified mode can be identified at the rim seal interface for the

3
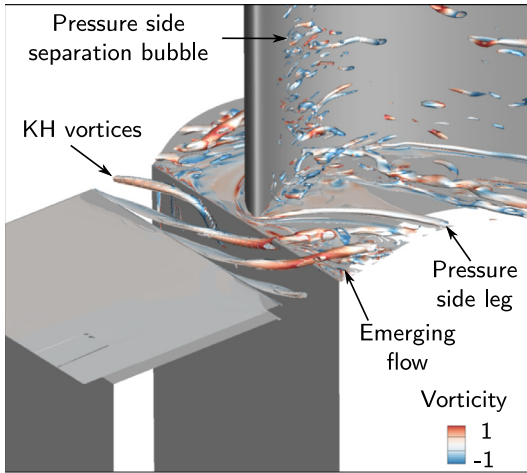
Fig. 17. Iso q-criterion $q = 10^6$ colored by the streamwise vorticity from an instantaneous LES2$_{\text{no inj.}}$ solution (b) with Kelvin–Helmholtz rolling structures, configuration A05.
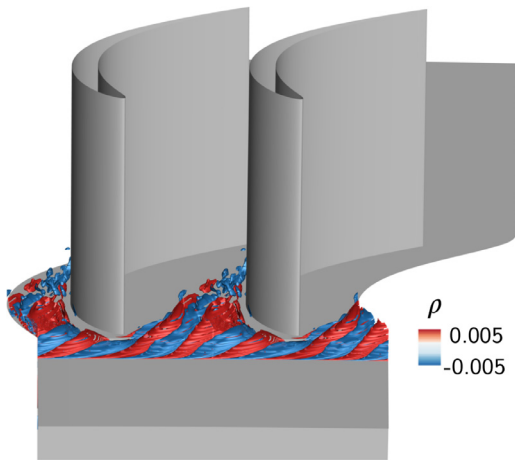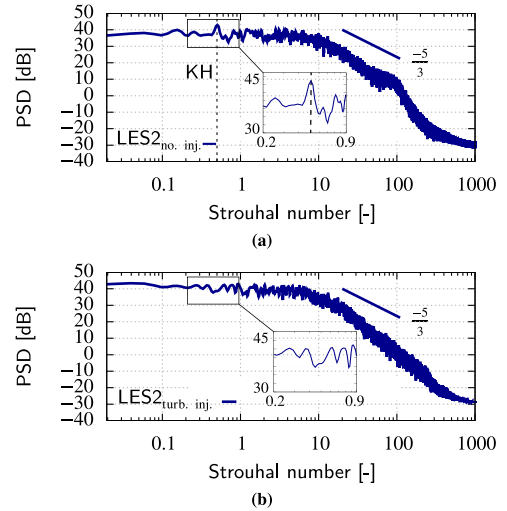

Fig. 18. Three-dimensional density modes related to Kelvin-Helmholtz instability based on fully three-dimensional DMD decomposition, configuration A05.
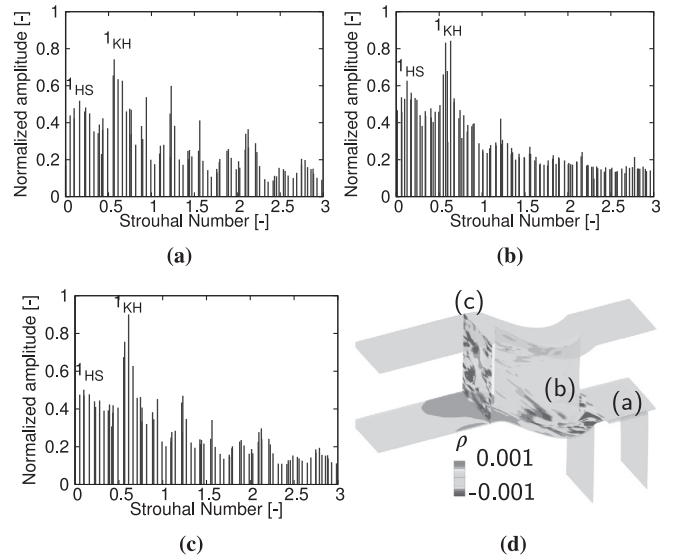

Fig. 19. Power spectral density (PSD) at the rim seal interface for the LES2$_{\text{no inj.}}$ (a) and LES2$_{\text{turb.inj.}}$ (b) simulations (see Fig. 11 for probe position), configuration A05. The dotted line indicates the Kelvin–Helmholtz characteristic frequency.

Fig. 20. Density frequency spectrum in x, z cuts and around the blade corresponding to the fundamental Kelvin–Helmholtz density mode for the LES2$_{\text{no inj.}}$, configuration A05.
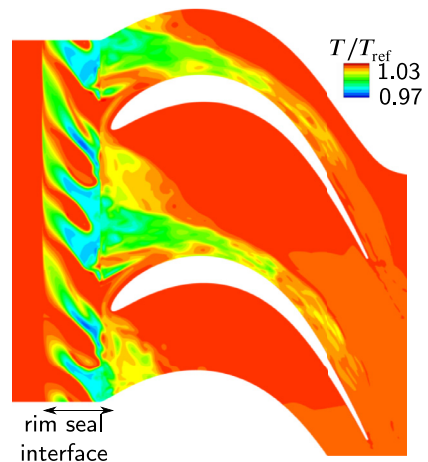
Fig. 21. Total temperature distribution at the hub from LES2$_{\text{no inj.}}$, configuration A05.

LES2$_{\text{turb inj.}}$ (see Fig. 19). This may be explained by the cancelling of this instability at a sufficiently high free-stream turbulence since a natural instability of the flow can be fully bypassed in relatively high free-stream turbulence similarly to the natural boundary layer transition bypassed by high free-stream turbulence [52].

5.2. Unsteady phenomena in the cascade

From the spectral content, the horse shoe vortex process and Kelvin–Helmholtz instability are the two main unsteady phenomena observed in the cascade for the LES2$_{\text{no inj.}}$ at the rim seal interface, around the blade and downstream of the blade (see Fig. 20) while only the horse shoe vortex process remains for the LES2$_{\text{turb. inj.}}$. Part of he main annulus flow is deviated downwards into the cavity when facing the blade potential effect. The mass balance for the cavity is fulfilled by some cavity flow blowing in the main annulus at the center of the inter-blade passage where potential effects are lower. This low momentum emerging flow is prone to be entrained by the pressure side leg of the horse shoe vortex process in a similar manner to the low momentum hub boundary layer. This phenomenon can be observed in Fig. 21 showing a temperature map close to the hub. Since the cavity flow is introduced with a lower temperature compared to the main annulus flow, this quantity can be used as a passive scalar of the mixing

Blade suction side

Shroud

Hub

$\frac{\sigma(p)}{p_{\text{ref}}}$ (%)

1
0.5

1 Passage vortex
2 Pressure side horse shoe vortex
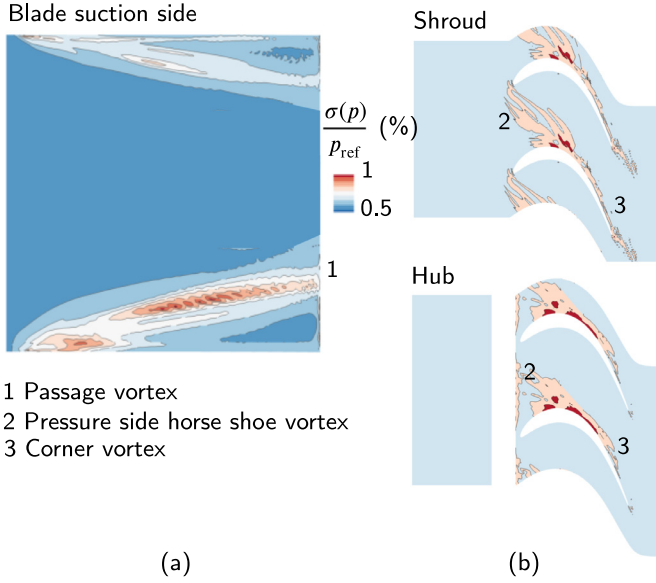3 Corner vortex

(a)   (b)

Fig. 22. Pressure standard deviation σ(p) around the blade suction side (a), at hub and shroud (b) for the LES2$_{\text{turb.inj.}}$, configuration A05.
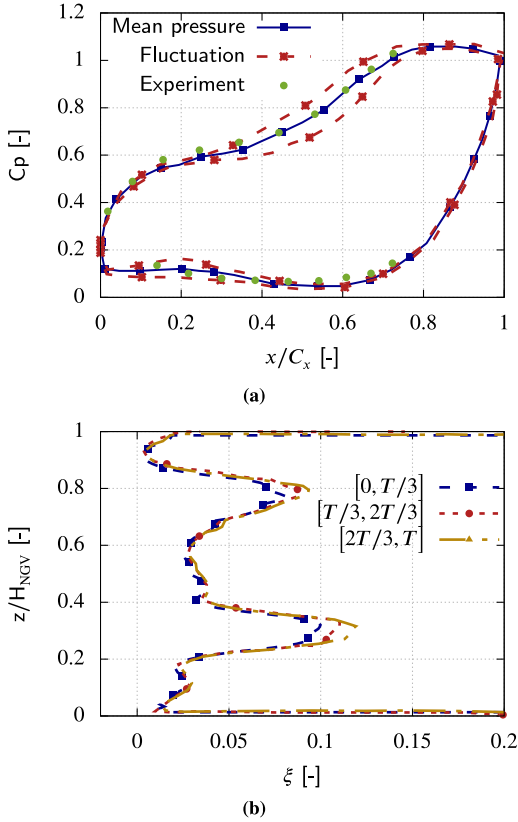

(a)

(b)

Fig. 23. Pressure coefficient and domain of fluctuation at 4% blade height (a) and downstream blade (b) where the period T corresponds to the characteristic period of time of the horse shoe vortex process for LES2$_{\text{turb.inj.}}$, configuration A05.

(a)

(b)

(c)

Fig. 24. Comparison of the pressure loss coefficient downstream of the blade for the standard and refined grids, configuration A05, (a) : RANS,(b) : LES elsA, (c) : LES AVBP.

of cavity flow with main annulus one. The cavity flow can be observed as travelling with the pressure side leg of the horse shoe vortex.

As stated, unlike the Kelvin–Helmholtz instability at the rim seal interface, the horse shoe vortex process is conserved independently of the free-stream turbulence. This corresponds to the periodical development of structures orthogonal to the flow that
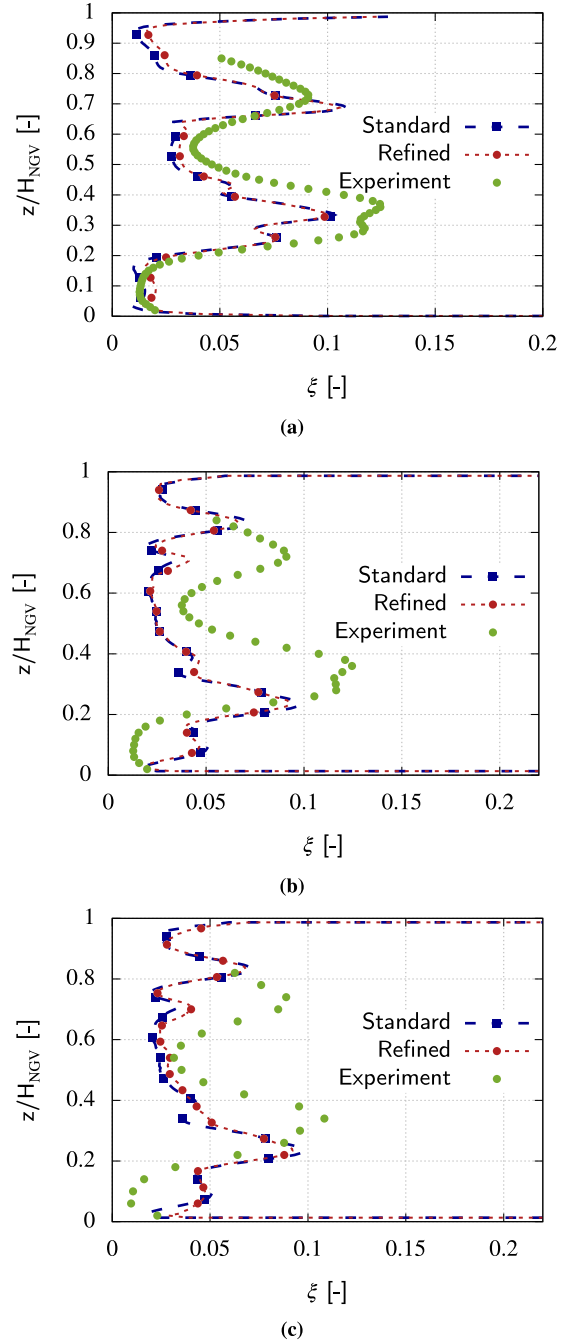
impact blade leading edge. A DMD performed at the shroud surface made possible to identify a few modes with a large amplification and related to the periodic horse shoe vortex development. The main harmonic of the phenomenon is set at Strouhal number St = $(f_r \text{ D})/u_{\text{edge}}$ = (250 0.02)/30 = 0.2 where f_r is the frequency, D the distance from saddle point to blade leading edge. The location where the horse shoe vortices develop and the pressure side leg of the horse shoe vortices migrate are associated to strong pressure standard deviation σ(p) on the hub and shroud (see Fig. 22 right). On the blade suction side, the strongest pressure deviations are observed where the passage vortices migrate (see Fig. 22 left). On the blade pressure side, the pressure fluctuations correspond to the separation bubble between $x/C_x = 0.1$ and $x/C_x = 0.3$ observed in-

dependently of the homogeneous or turbulence injection at the inlet of the domain (see Fig. 23a). Even downstream of the blade, the pressure loss coefficient experiences amplitude fluctuations in particular in regions of strong losses related to the passage vortices (see Fig. 23b).

6. Conclusion

The effect of turbulence on the physical phenomena observed in a linear cascade with upstream hub cavity has been assessed by comparing RANS, LES and LES with inlet turbulence injection. In conjunction with experiments, the numerical results show that the hub and shroud boundary layers approaching the blade leading edge turn turbulent under a bypass process due to the free-stream turbulence. The main effects are a stronger migration towards midspan of the hub and shroud passage vortices compared to a laminar boundary layer. Also, the suction side boundary layer is allegedly to become transitional/turbulent. This information is supported based on the suction side separation bubble (observed in the LES without turbulence injection) while cancelled in the LES with turbulence injection due to the turbulent nature of the boundary layer. The description of the flow field in the cavity shows an entrainment effect of the high momentum main annulus flow on the cavity flow with local recirculation zones in the rim seal for overlapping geometries promoting a reduced shear layer at the rim seal interface. The main sources of unsteadiness observed in the linear cascade are the horse shoe vortex process, trailing shed and Kelvin-Helmholtz instability at the rim seal interface due to shear layer. This last natural instability is observed only at low free-stream turbulence (LES without turbulence injection) while cancelled at higher free-stream turbulence (LES with inlet turbulence injection).

Declaration of Competing Interest

The authors declare that they have no known competing financial interests or personal relationships that could have appeared to influence the work reported in this paper.

Acknowledgments

Appendix A. Mesh dependency

The assessment of the grid convergence for the different approaches is made by comparing the pressure loss coefficient downstream of the blade for two level of mesh refinement. The first mesh is the one used during this study and a second mesh that is refined. For the RANS approach, the additional grid has been generated with reduced characteristic mesh lengths in the transverse directions (x,z) and the expansion ratio in the wall-normal direction has been also decreased to 1.1. For the pressure loss coefficient downstream of the blade, a similar local discrepancy can be observed especially in the two main peaks of loss in the order of magnitude of 2%. However, the results for the standard and fine grids are in good agreement to indicate grid convergence. For the LES simulation based on structured grid, the mesh

has been refined by decreasing all three near-wall characteristic lengths: $\Delta x^+ \leq 60$, $y_1^+ \leq 0.8$ and $\Delta z^+ \leq 15$. The mesh refinement has been mainly performed in the spanwise direction. This parameter have been shown to strongly influence LES simulation quality [27] and fewer in the streamwise direction since the streaks that are to be captured in wall-resolved LES simulations are elongated structures in the streamwise direction [1] with fewer variations in the stream direction. The final mesh is composed of around 110×10^6 cells compared to the 60×10^6 cells mesh used for the study. For the LES on unstructured grid approach, the mesh has been refined in the wall-normal direction to reach $y_1^+ \simeq 1$ and the triangle discretization on surfaces have been decreased compared to the standard grid used for the study. Fig. 24 shows the comparison of pressure distribution downstream blade for the configuration A05 for the different LES approaches with the two mesh refinement. The change in mesh size shows local discrepancy in the order of magnitude of 4% in loss peak region for the elsA and AVBP approaches. Despite these local differences, the results between standard and refined meshes are in good agreement.

References

[1] Tucker PG. Computation of unsteady turbomachinery flows: part 2-LES and hybrids. Prog Aerosp Sci 2011;47(7):546–69. doi:10.1016/j.paerosci.2011.07.002.

[2] Hourmouziadis J. Aerodynamic design of low pressure turbines. AGARD Lect Ser 1989;167(167).

[3] Mayle RE. The role of laminar-turbulent transition in gas turbine engines. Volume 5: manufacturing materials and metallurgy; ceramics; structures and dynamics; controls, diagnostics and instrumentation; education; IGTI scholar award; general; 1991. ISBN 978-0-7918-7902-3. doi:10.1115/91-GT-261.

[4] Abu-Ghannam BJ, Shaw R. Natural transition of boundary layersâthe effects of turbulence, pressure gradient, and flow history. J Mech Eng Sci 1980;22(5):213–28.

[5] Hodson HP, Howell RJ. Blade row interaction, transition, and high-lift airfoils in low-pressure turbine. Annu Rev Fluid Mech 2005;37(1):71–98. doi:10.1146/annurev.fluid.37.061903.175511.

[6] Cui J, Nagabhushana Rao V, Tucker PG. Numerical investigation of contrasting flow physics in different zones of a high-Lift low-Pressure turbine blade. J Turbomach 2015;138(1):11003. doi:10.1115/1.4031561.

[7] Gier J, Franke M, Hübner N, Schröder T. Designing low pressure turbines for optimized airfoil lift. J Turbomach 2010. doi:10.1115/1.3148476.

[8] Jones W, Launder B. The prediction of laminarization with a two-equation model of turbulence. Int J Heat Mass Transf 1972;15(2):301–14. doi:10.1016/0017-9310(72)90076-2.

[9] Menter FR, Langtry R, Völker S, Huang PG. Transition modelling for general purpose CFD codes. Engineering turbulence modelling and experiments 6; 2005. doi:10.1016/B978-008044544-1/50003-0.

[10] Sagaut P. Large eddy simulation for incompressible flows: an introduction; 2006. doi:10.1007/b137536.

[11] Wu X, Durbin PA. Evidence of longitudinal vortices evolved from distorted wakes in a turbine passage. J Fluid Mech 2001;446:199–228. doi:10.1017/S0022112001005717.

[12] Michelassi V, Wissink J, Rodi W. Analysis of DNS and LES of flow in a low pressure turbine cascade with incoming wakes and comparison with experiments. Flow Turbul Combust 2002;69(3–4):295–330. doi:10.1023/A:1027334303200.

[13] Wissink JG, Rodi W. Direct numerical simulation of flow and heat transfer in a turbine cascade with incoming wakes. J Fluid Mech 2006;569:209–47. doi:10.1017/S002211200600262X.

[14] Raverdy B, Mary I, Sagaut P, Liamis N. High-resolution large-Eddy simulation of flow around low-Pressure turbine blade. AIAA J 2008. doi:10.2514/2.1989.

[15] Lengani D, Simoni D, Pichler R, Sandberg R, Michelassi V. On the identification and decomposition of the unsteady losses in a turbine cascade. In: Proceedings of ASME Turbo Expo 2018; 2018. https://doi.org/10.1115/1.4042164.

[16] Marconcini M, Pacciani R, Arnone A, Michelassi V, Pichler R, Zhao Y, et al. Large eddy simulation and RANS analysis of the end-Wall flow in a linear low-Pressure-Turbine cascade - Part II: loss generation. J Turbomach 2018. doi:10.1115/1.4042208.

[17] Tyacke JC, Tucker PG, Jefferson-Loveday R, Vadlamani NR, Watson R, Naqvi I, et al. Large eddy simulation for turbines: methodologies, cost and future outlooks. J Turbomach 2014. doi:10.1115/1.4025589.

[18] Tyacke JC, Tucker PG. Future use of large eddy simulation in aeroengines. J Turbomach 2015;137(August):GT2014–25434. doi:10.1115/1.4029363.

[19] Cui J, Tucker P. Numerical study of purge and secondary flows in a low-Pressure turbine. J Turbomach 2016. doi:10.1115/1.4034684.

[20] Hammer F, Sandham N, Sandberg R. The influence of different wake profiles on losses in a low pressure turbine cascade. Int J Turbomach Propul Power 2018. doi:10.3390/ijtpp3020010.

[21] Sandberg RD, Michelassi V, Pichler R, Chen L, Johnstone R. Compressible direct numerical simulation of low-pressure turbines-part i: methodology. J Turbomach 2015. doi:10.1115/1.4028731.

[22] Michelassi V, Chen L-W, Pichler R, Sandberg RD. Compressible direct numerical simulation of low-Pressure turbines-Part II: effect of inflow disturbances. J Turbomach 2015;137(7):71005. doi:10.1115/1.4029126.

[23] Schuler P, Dullenkopf K, Bauer H-J. Investigation of the influence of different rim seal geometries in a low-Pressure turbine. In: Volume 7: Turbomachinery, Parts A, B, and C; 2011. p. 715–29. doi:10.1115/GT2011-45682.

[24] Cambier L, Veuillot J. Status of the elsA software for flow simulation and multi-disciplinary applications. In: 46th AIAA aerospace sciences meeting and exhibit; 2008. p. 664. doi:10.2514/6.2008-664.

[25] Gourdain N, Sicot F, Duchaine F, Gicquel L. Large eddy simulation of flows in industrial compressors: a path from 2015 to 2035. Phil Trans R Soc A 2014;372(2022):20130323. doi:10.1098/rsta.2013.0323.

[26] Piomelli U. Wall-layer models for large-eddy simulations. Prog Aerosp Sci 2008;44(6):437–46. doi:10.1016/j.paerosci.2008.06.001.

[27] Pichler R, Zhao Y, Sandberg RD, Michelassi V, Pacciani R, Marconcini M, et al. LES and RANS analysis of the end-wall flow in a linear LPT cascade with variable inlet conditions, Part I: Flow and secondary vorticity fields. In: ASME Turbo Expo 2018: turbomachinery technical conference and exposition. Oslo, Norway; 2018. https://doi.org/10.1115/GT2018-76450.

[28] Gicquel LYM, Gourdain N, Boussuge J-F, Deniau H, Staffelbach G, Wolf P, et al. High performance parallel computing of flows in complex geometries. Comptes Rendus Mécanique 2011;339(2–3):104–24. doi:10.1016/j.crme.2010.11.006.

[29] Nishikawa H, Rad M, Roe P. A third-order fluctuation splitting scheme that preserves potential flow. In: 15th AIAA Computational Fluid Dynamics Conference; 2013. https://doi.org/10.2514/6.2001-2595.

[30] Wilcox DC. Formulation of the k-ω turbulence model revisited. AIAA J 2008. doi:10.2514/1.36541.

[31] Gourdain N. Prediction of the unsteady turbulent flow in an axial compressor stage. part 1: comparison of unsteady RANS and LES with experiments. Comput Fluids 2015. doi:10.1016/j.compfluid.2014.09.052.

[32] Gourdain N. Prediction of the unsteady turbulent flow in an axial compressor stage. part 2: analysis of unsteady RANS and LES data. Comput Fluids 2015. doi:10.1016/j.compfluid.2014.09.044.

[33] Jameson A, Schmidt W, Turkel E. Numerical solutions of the euler equations by finite volume methods using runge-Kutta time-stepping schemes. AIAA paper; 1981. doi:10.2514/6.1981-1259.

[34] Marmignon C, Couaillier V, Courbet B. Solution strategies for integration of semi-Discretized flow equations in elsa and CEDRE. AerospaceLab J 2011.

[35] Nicoud F, Ducros F. Subgrid-scale stress modelling based on the square of the velocity gradient tensor. Flow Turbul Combus 1999;62(3):183–200. doi:10.1023/A:1009995426001.

[36] Colin O, Rudgyard M. Development of high-Order taylor-Galerkin schemes for LES. J Comput Phys 2000;162(2):338–71. doi:10.1006/jcph.2000.6538.

[37] Odier N, Sanjosé M, Gicquel L, Poinsot T, Moreau S, Duchaine F. A characteristic inlet boundary condition for compressible, turbulent, multispecies turbomachinery flows. Comput Fluids 2018. doi:10.1016/j.compfluid.2018.09.014.

[38] Smirnov A, Shi S, Celik I. Random Flow Simulations with Bubble Dynamics Model. In: Proceedings of FEDSM00 ASME 2000 fluids engineering division summer meeting, FEDSM2000-; 2000.

[39] Fontaneto F. Aero-thermal performance of a film-cooled high pressure turbine blade/vane: a test case for numerical codes validation; 2014.

[40] Troth LS. Multi-physics coupled simulation of gas turbine; 2017.

[41] Jonáš P, Mazur O, Uruba V. On the receptivity of the by-pass transition to the length scale of the outer stream turbulence. Eur J Mech B/Fluids 2000. doi:10.1016/S0997-7546(00)01094-3.

[42] Passot T, Pouquet A. Numerical simulation of compressible homogeneous flows in the turbulent regime. J Fluid Mech 1987. doi:10.1017/S0022112087002167.

[43] Sagaut P, Cambon C. Homogeneous turbulence dynamics; 2018. ISBN 978-3-319-73162-9. doi:10.1007/978-3-319-73162-9.

[44] Barenblatt GI. Scaling laws for fully developed turbulent shear flows. part 1. basic hypotheses and analysis. J Fluid Mech 1993. doi:10.1017/S0022112093000874.

[45] Schulte V, Hodson HP. Unsteady wake-Induced boundary layer transition in high lift LP turbines. J Turbomach 2011. doi:10.1115/1.2841384.

[46] Coull JD, Hodson HP. Unsteady boundary-layer transition in low-pressure turbines. J Fluid Mech 2011. doi:10.1017/jfm.2011.204.

[47] Hodson HP, Dominy RG. Three-Dimensional flow in a low-Pressure turbine cascade at its design condition. J Turbomach 1987;109(2):177. doi:10.1115/1.3262083.

[48] Kost F, Nicklas M. Film-cooled turbine endwall in a transonic flow field: part I - Aerodynamic measurements. J Turbomach 2001;123(4):709–19. doi:10.1115/1.1400112.

[49] Sharma OP, Butler TL. Predictions of endwall losses and secondary flows in axial flow turbine cascades. J Turbomach 1987;109(86):229. doi:10.1115/1.3262089.

[50] Sieverding CH. Recent progress in the understanding of basic aspects of secondary flows in turbine blade passages. J Eng Gas Turbine Power 1985;107(2):248. doi:10.1115/1.3239704.

[51] Schmid PJ, Li L, Juniper MP, Pust O. Applications of the dynamic mode decomposition. Theor Comput Fluid Dyn 2011. doi:10.1007/s00162-010-0203-9.

[52] Hosseinverdi S, Fasel HF. Laminar-turbulent transition in a laminar separation bubble in the presence of free-stream turbulence. Procedia IUTAM; 2015. doi:10.1016/j.piutam.2015.03.066.